ACS APPLIED MATERIALS & INTERFACES

www.acsami.org

Research Article

Toward Optical Detection of Single Chiral Molecules Using Magneto-Optical Hyperbolic Metasurfaces

William O F Carvalho,* Ana L Lyra Pavanelli, Osvaldo N. Oliveira, Jr., and Jorge R Mejía-Salazar*

Cite This: *ACS Appl. Mater. Interfaces* 2025, 17, 57719−57726

Read Online

ACCESS | Metrics & More | Article Recommendations | Supporting Information

ABSTRACT: Chiral molecule detection is normally made with circular dichroism spectroscopy, which often requires high analyte concentrations or large sample volumes. This study proposes an optical metasurface architecture consisting of nanodisks made from magneto-optical hyperbolic metamaterials, which enables detection of single chiral molecules. The nanodisks are engineered from alternating layers of metallic and magneto-optical dielectric materials, forming two-dimensional gratings that eliminate the need for traditional prism coupling. When phase-matching conditions are met, incident light couples into bulk plasmon-polariton modes —whose resonantly enhanced and localized electromagnetic fields are highly responsive to changes in the surrounding medium. Chiral sensing is enabled by applying a magnetic field in the polar configuration, which induces differences in the reflection of left- and right-handed circularly polarized light, producing a measurable magnetic circular dichroism (MCD) signal. Two complementary MCD-based sensing strategies are demonstrated: refractometric detection of achiral analytes and chiroptical sensing of chiral molecules. The refractometric approach achieves an MCD sensitivity of $S = 245$ nm·RIU^{-1}, while the chiroptical method enables detection at ultralow concentrations, with MCD peak values of $|MCD_p| = 4.71°$, $|MCD_p| = 2.41°$, and $|MCD_p| = 2.36°$, corresponding to concentration ratios of four, two, and one molecule per unit cell, respectively. These results highlight the concept here as a platform for label-free chiral biosensing.

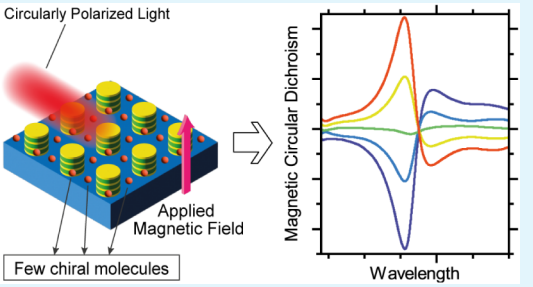

KEYWORDS: *chiral Biosensing, few-molecule sensing, hyperbolic metamaterials, magnetochiroptical Sensing, magnetic Circular Dichroism, metasurfaces*

1. INTRODUCTION

Chirality is a geometric property that prevents an object from being superimposed onto its mirror image, regardless of any transformation. A familiar example is our hands—they are mirror images but cannot be perfectly aligned. Chirality is also fundamental in biochemistry, appearing in amino acids, carbohydrates, lipids, and even entire organisms, being essential in biological and pharmacological processes. In an achiral environment, the enantiomers of a chiral molecule exhibit identical physicochemical properties, but this is not so in chiral settings such as the human body. Their properties can differ significantly, influencing biochemical interactions and drug responses.[1,2] Indeed, alterations in the chirality of biomolecules, such as proteins, have been linked to neurodegenerative disorders, including Alzheimer's and Parkinson's diseases.[3] The recognition and separation of enantiomers are therefore important for the pharmaceutical industry, where enantiopure drugs are favored to enhance bioavailability, metabolism, excretion, and potency, while also improving safety and cost efficiency.[4−7] Molecular chirality is normally determined using circular dichroism (CD) measurements. This technique is limited to high concentrations or large analyte volumes, owing to the weak molecular-chiroptical activity caused by the mismatch in size between the molecule and the optical wavelengths. Hence, CD cannot be used to analyze few particles or a single molecule.[8,9] It is possible to increase sensitivity by engineering the shape and material composition of plasmonic nanoparticles to enhance chiroptical light-matter interactions with the intense localized electromagnetic near fields associated with plasmonic resonances at metal/dielectric interfaces.[10−15] Even with such advancements, detecting a few molecules with existing approaches often requires fluorescent labels[16] or quantum metrology techniques.[17] These methods have their own limitations: fluorescent labeling can compromise the primary advantage of label-free plasmonic biosensing—real-time monitoring of binding events—while quantum techniques rely on delicate quantum states, demanding additional preparation steps and specialized, often costly, equipment.

An alternative to the plasmonic systems for chiral molecule sensing are the magneto-optical (MO) chiral metasurfaces, also

Received: August 12, 2025
Revised: September 23, 2025
Accepted: September 27, 2025
Published: October 3, 2025

https://doi.org/10.1021/acsami.5c16043
ACS Appl. Mater. Interfaces 2025, 17, 57719−57726

known as magnetochiroptical metasurfaces.[18,19] These metasurfaces comprise two-dimensional arrays of elementary ferromagnetic resonators, whose intrinsic magnetization—in the polar configuration (i.e., aligned parallel to the propagation of light)—can be controlled dynamically. Under an external magnetic field, the magnetization can be tuned to align either parallel or antiparallel to the wavevector of the incident electromagnetic wave. This magnetic control induces polarization rotations—chiral interactions—through the Faraday effect in transmission and the polar magneto-optical Kerr effect in reflection. As a result, these metasurfaces enable fine-tuned manipulation of far-field chiral features via strong near-field magnetochiroptical interactions along the metasurface.[20−22] This latter capability is the foundation of nanophotonic-based chiral biosensing. When a chiral molecule interacts with chiral near-fields, the resulting chiral-optical-matter interaction induces measurable changes in far-field optical features. These changes not only indicate the presence of chiral matter but also allow for precise quantification, as their magnitude is proportional to the amount of chiral matter engaged with the near-field.[23−27] The theoretical approach integrating magneto-chiroptical near-field interactions with high-field confinement in a two-dimensional array of cavities within a hyperbolic metamaterial (HMM) predicts an exceptional sensitivity with detection of as few as 20 nanoparticles within each nanocavity.[28] However, further advancements are required to enable detection at even smaller numbers of particles, which remains a significant challenge.

In this work, we propose a metasurface made of MO-HMM nanodisks, structured with alternating layers of dielectric-ferromagnetic and metallic materials. This concept builds upon recent demonstrations of MO activity in nonmagnetic HMM nanodisks composed solely of dielectric and metallic layers.[29] However, in contrast to these earlier approaches, our design exploits the intrinsic magnetization of the ferromagnetic components to actively modulate the polarization state of incident light. This magnetization can be reversed dynamically via external magnetic fields, thus permitting a range of tunable optical functionalities. Here, we focus on the sensing of chiral nanoparticles such as chiral biomolecules, with emphasis on a magnetization configuration perpendicular to the metasurface plane. This setup induces magneto-chiroptical effects, enhancing the system's chiral sensing capabilities. A key advantage of this mechanism is the phase-matching condition governed by the two-dimensional arrangement of MO-HMM nanocylinders. These act as grating couplers, removing the need for external prism couplers. When exposed to an applied magnetic field, the metasurface exhibits distinct reflectance responses based on the circular polarization (CP) of the incident light. These polarization-dependent variations can be measured via magnetic CD (MCD), allowing the detection of small changes in refractive index—observed as wavelength shifts in the MCD peak—and molecular chirality, indicated by variations in MCD amplitude. We shall show that the proposed metasurface achieves high sensitivity for both refractive index sensing in achiral environments and of chiral nanoparticles. In the latter case, it may represent a breakthrough in label-free chiral biosensing.

2. METHODOLOGY

Figure 1a illustrates the metasurface proposed, consisting of a two-dimensional square-lattice structure of MO-HMM nanocylinders grown on a silica (SiO_2) substrate. The cylinders are

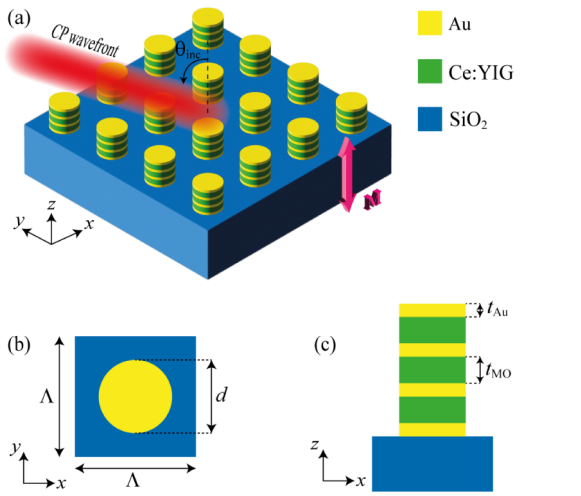

Figure 1. (a) Schematic representation of the metasurface with MO-HMM cylinders. The geometrical parameters are given in (b) upper and (c) cross-section views.

uniformly distributed along the *xy*-plane with a periodicity Λ. Each nanocylinder comprises an alternating stack of gold (Au) and cerium-substituted yttrium iron garnet (Ce:YIG) nanodisks. Figures 1b−(c show the top and side views of the unit cell, respectively. The stacked nanodisks have a uniform diameter *d*, with all Au layers having a constant thickness t_{Au}, while the Ce:YIG layers have a thickness t_{MO}. Our design is compatible with well-established thin-film deposition techniques, including electron-beam evaporation, sputtering, and pulsed laser deposition (PLD), combined with advanced lithographic methods such as electron-beam lithography (EBL), focused ion beam (FIB) lithography, or nanoimprint lithography, followed by etching or liftoff processes to pattern the multilayered stack into nanodisk arrays.[30,31] The metasurface is considered immersed in an aqueous superstrate, which serves as the analyte medium. It acts as a two-dimensional grating coupler, which simplifies device architecture by eliminating the need for a prism coupler. Under phase-matching conditions, the incident wave couples resonantly with surface modes along the metasurface, resulting in minima in reflectance amplitudes. These surface modes are highly sensitive to the resonant properties of the HMM nanocylinders. The alternate stacking of dielectric and metallic layers gives rise to intrinsic plasmonic resonances, some of which occur at wavelengths considerably larger than the thickness of individual layers. Unlike conventional surface plasmon-polariton modes, these resonances exhibit enhanced and localized electromagnetic fields that extend throughout the entire volume of the structure rather than being confined to a single surface. These volumetric modes are commonly referred to as volume plasmon-polaritons (VPP) or bulk plasmon-polariton (BPP) modes.[28]

We analyze a CP optical field impinging from the superstrate (represented by the red beam in Figure 1a) at an angle θ_{inc} within the *xz*-plane. The magnetization state of the MO Ce:YIG material is illustrated by the vector **M** (pink arrow), oriented along the ± *z*-axis. For $\theta = 0°$, the system is in a polar configuration. However, when $0° < \theta < 90°$, **M** induces magneto-optical polarization rotations due to its coupling with the wavevector component along the *z*-axis (k_z). The magnetization state can be manipulated actively by an applied magnetic field, which modifies the magnetization state of the

https://doi.org/10.1021/acsami.5c16043
ACS Appl. Mater. Interfaces 2025, 17, 57719−57726

MO Ce:YIG material, thereby modulating the reflected wavefronts. This effect can be analyzed quantitatively through the MCD parameter (in degrees)[4]

$$\mathrm{MCD}\ (^\circ) = \tan^{-1}\left(\frac{R_{\mathrm{RCP}} - R_{\mathrm{LCP}}}{R_{\mathrm{RCP}} + R_{\mathrm{LCP}}}\right) \tag{1}$$

where R_{RCP} and R_{LCP} are the reflectances for right-handed CP (RCP) and left-handed CP (LCP) lights, respectively. In this configuration with **M** oriented along the $\pm z$-axis, the permittivity tensor has nonzero off-diagonal elements for the Ce:YIG material, given by[32]

$$\tilde{\varepsilon}_{\mathrm{MO}}(\lambda) = \begin{pmatrix} \varepsilon_{\mathrm{MO}}(\lambda) & im\varepsilon_{xy}(\lambda) & 0 \\ -im\varepsilon_{yx}(\lambda) & \varepsilon_{\mathrm{MO}}(\lambda) & 0 \\ 0 & 0 & \varepsilon_{\mathrm{MO}}(\lambda) \end{pmatrix} \tag{2}$$

with $\varepsilon_{\mathrm{MO}}$ and $\varepsilon_{xy} = \varepsilon_{yz}$ for the complex diagonal and off-diagonal components of the permittivity tensor, respectively, both dependent on the incident wavelength λ. The parameter $m = \pm 1$ indicates the direction of magnetization along the z-axis. For Ce:YIG, we used off-diagonal permittivity values from experimental data[32] obtained under magnetization saturation for an external magnetic field of approximately $B = 2$ kOe. Similarly, the permittivity values for Au[33] and SiO_2[34] were taken from experimental data.

The alternating stack of Ce:YIG and Au layers can sustain BPP modes owing to their distinctive hyperbolic dispersion properties. Specifically, the effective permittivity components—perpendicular ($\varepsilon_\perp$) and parallel ($\varepsilon_\parallel$)— meet the condition $\varepsilon_\parallel\varepsilon_\perp < 0$.[35] This implies that the nanocylinders exhibit metallic behavior along one axis while acting as a dielectric along another, which explains the electromagnetic field confinement in the volume of the structure. The effective medium works perfectly for an infinite repetition of the alternating dielectric/metallic cycle, but the hyperbolic behavior prevails when the system contains only a few cycles. Indeed, the electromagnetic properties of finite HMMs can be described by the expressions,[29,35,36]

$$\varepsilon_\perp(\lambda) = \frac{\varepsilon_{\mathrm{MO}}(\lambda)\varepsilon_{\mathrm{Au}}(\lambda)(t_{\mathrm{MO}} + t_{\mathrm{Au}})}{t_{\mathrm{MO}}\varepsilon_{\mathrm{MO}}(\lambda) + t_{\mathrm{Au}}\varepsilon_{\mathrm{Au}}(\lambda)} \tag{3}$$

and

$$\varepsilon_\parallel(\lambda) = \frac{t_{\mathrm{MO}}\varepsilon_{\mathrm{MO}}(\lambda) + t_{\mathrm{Au}}\varepsilon_{\mathrm{Au}}(\lambda)}{t_{\mathrm{MO}} + t_{\mathrm{Au}}} \tag{4}$$

All simulations were conducted using the finite element method (FEM) in COMSOL Multiphysics. To model an infinitely periodic two-dimensional system, Floquet periodic boundary conditions were applied along the xy-plane, enabling infinite repetition of a single unit cell. At the z-boundaries, perfectly matched layers (PMLs) were implemented to suppress spurious reflections. Numerical results were computed for wavelengths ranging from 700 nm $\leq \lambda \leq$ 900 nm and an oblique incidence angle of $\theta_{\mathrm{inc}} = 35^\circ$.

3. RESULTS AND DISCUSSION

The goal of this study is to design a metasurface composed of hyperbolic-material nanocylinders to exhibit two key phenomena: surface modes excited through diffractive coupling and BPP modes associated with hyperbolic dispersion. To achieve this, we employed an optimization algorithm integrated within the COMSOL Multiphysics software. This algorithm automatically sweeps through the geometric parameters to identify the optimal configuration that simultaneously satisfies both desired conditions: the excitation of surface modes via diffractive coupling and the presence of BPP modes. This systematic approach ensures precise tuning of the metasurface's optical response, enhancing its overall performance and functionality. In particular, we performed all these geometrical optimization process for the system working for incident wavelengths centered around $\lambda = 790$ nm. More specifically, within the range from 760 nm up to 820 nm. This wavelength range was chosen due to the strong magneto-optical (MO) response of the Ce:YIG material. From the automated optimization process, we obtained HMM nanodisks comprising four gold nanodisks ($t_{\mathrm{Au}} = 20$ nm each) alternating with three Ce:YIG nanodisks ($t_{\mathrm{MO}} = 40$ nm each) having a diameter of $d = 200$ nm, and arranged with a periodicity of $\Lambda = 330$ nm, as depicted in Figure 1a–c. The initial optimization process was conducted without accounting for MO effects, prioritizing the excitation of BPPs. Subsequently, all simulations hereafter incorporate MO effects using eq 2, with **M** configured in a polar orientation (as illustrated in Figure 1a) to enable active modulation of RCP and LCP waves.

3.1. Refractometric Sensing of Achiral Analytes. A key question is whether the proposed metasurface can detect analytes by simply observing dips in the reflection spectra, similar to conventional grating-based sensors and biosensors. The answer is no as we verified by examining the sensing mechanism associated with achiral analytes. Although not shown here, our numerical results for the reflectance dips corresponding to different refractive index concentrations revealed a significant overlap among broad, closely spaced dips. This overlap severely limits resolution, making the approach unsuitable for sensing and biosensing applications. We have therefore focused on the influence of refractive index variations in the surrounding aqueous medium on the MCD of the HMM nanocylinders. In our analysis, we assume homogeneous refractive index changes in the aqueous medium, with the analyte refractive index (n_a) varying within the range $1.33 \leq n_a \leq 1.38$. This interval of refractive index changes was specifically chosen because it corresponds to the region where the MCD response exhibits a well-defined linear sensitivity to refractive index changes, making it optimal for reliable sensing performance.

Figure 2a shows numerical results for the reflectance associated with RCP (R_{RCP}) and LCP (R_{LCP}) incident waves, with magnetization aligned along the + z-direction, i.e., for $m = +1$ in eq 2. The inset of Figure 2a provides a closer view of the reflectance minimum, revealing a slight difference between R_{RCP} and R_{LCP}, which gives rise to the MCD response shown in purple-solid curve in Figure 2b. Note that the MCD response exhibits a sharper spectral profile than the reflectance spectra, making it advantageous for a higher resolution plasmonic biosensing approach. Moreover, the MCD approach yields an amplitude enhancement by a factor of 4.4 compared to the maximum CD response of the nonmagnetized structure ($m = 0$), for which CD = −0.04923°. It is worth mentioning that the MCD peak, with an amplitude of $\mathrm{MCD_p} = -0.216^\circ$ at $\lambda = 783$ nm, is associated with the modulation of the BPP mode in the structure, as expected from our optimized numerical design. Importantly, numerical results in this last figure indicate that beyond the sensing applications discussed in this work, the proposed MO-HMM metasurface also holds potential for

https://doi.org/10.1021/acsami.5c16043
ACS Appl. Mater. Interfaces 2025, 17, 57719−57726

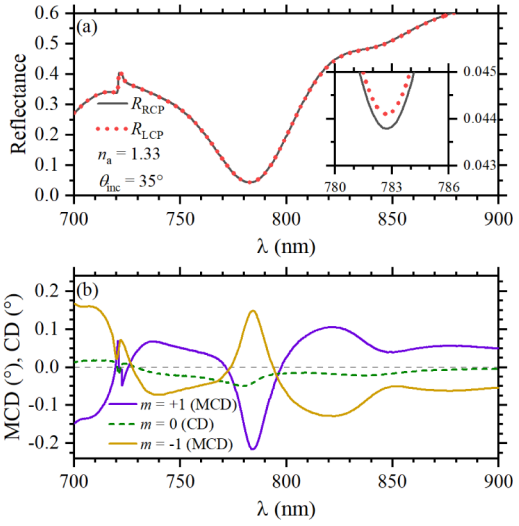

Figure 2. (a) Reflectance spectra of the metasurface for RCP (black-solid) and LCP (red-dotted) incident wavefronts for m = +1, with a small discrepancy at the resonant BPP coupling (inset). (b) MCDs and CD calculated with eq 1, for m = +1 (purple-solid), m = −1 (yellow-solid), and m = 0 (green-dashed).

active manipulation of the polarization state of incident light. This capability is illustrated in Figure S1, where extrinsic chirality and combined extrinsic-magneto-chiroptical effects are exploited to alter, and in some cases completely flip, the incident polarization. This phenomenon is predominantly governed by near-field interactions determined by the symmetry of the bulk plasmon polariton (BPP) modes supported by the structure, as further evidenced in Figures S2a and b for the RCP and LCP incident fields.

As already mentioned, a key characteristic of BPP modes is their electromagnetic field distribution throughout the volume of the HMM structure—in this case, the HMM cylinders. To verify this property for the mode excited at λ = 783 nm, which corresponds to the reflectance minimum in Figure 2a, we analyze the electromagnetic near-field distributions at this resonant wavelength. Figures 3a, c, and e present the normalized electric near-field profiles, while Figure 3b, d, and f display the corresponding normalized magnetic near-field distributions. These fields are mapped along the *xy*, *xz*, and *yz* planes, respectively. The results confirm the expected electromagnetic near-field distribution, demonstrating a collective plasmon excitation throughout the structure. Additionally, due to the finite size of the plasmonic nanoparticles (in contrast to infinite two-dimensional layers,[36] the system exhibits hybrid features associated with localized surface plasmon-polariton modes. This is evident from the enhanced and localized electromagnetic near-fields along the lateral sides of Au nanodisks, as noticed from Figure 3c and e.

Similarly to conventional plasmonic biosensing approaches, the enhanced, localized near-fields around HMM nanocylinders are expected to be highly sensitive to the dielectric properties of the surrounding medium.[24] Therefore, we now assess the feasibility of monitoring refractive index changes induced by achiral analytes. Figure 4a shows MCD curves for different refractive indices within the range of interest. There is a clear redshift trend as n_a increases. This behavior is further analyzed in Figure 4b, where the MCD dip positions are plotted as a function of n_a, revealing an almost linear relationship with minor fluctuations up to n_a = 1.38. As

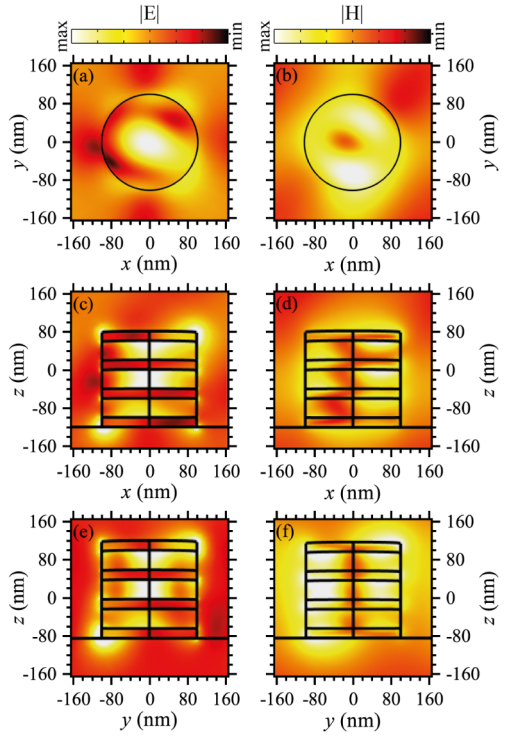

Figure 3. Normalized E and H near-field profiles at resonant BPP coupling at 783 nm seen in (a)−(b) *xy*-plane, (c)−(d) *xz*-plane and (e)−(f) *yz*-plane.

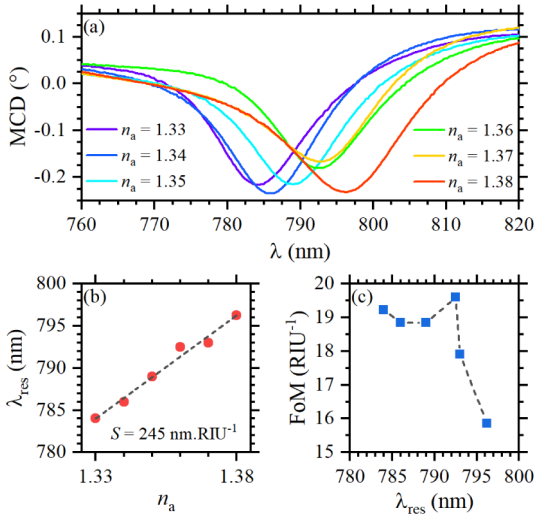

Figure 4. (a) MCD responses with n_a and the corresponding (b) linear sensitivity of S = 245 nm·RIU^{-1}. (c) Small variation of FoM as a function of MCD peaks.

mentioned earlier, for n_a > 1.38, the sensitivity deviates from linearity. This deviation can be attributed to the reduced refractive index contrast between the superstrate and substrate, which alters the phase-matching conditions required for efficient excitation of plasmonic modes in the metasurface. The slope of the linear regression yields a sensitivity of S = 245 nm·RIU^{-1}, which is highly competitive with recent approaches.[28] However, despite this high sensitivity, the resolution of this approach remains limited, as evidenced by the low values of the figure-of-merit (FoM) in Figure 4c. The FoM (S/Γ), which relates the sensitivity (S) to line width (Γ)

https://doi.org/10.1021/acsami.5c16043
ACS Appl. Mater. Interfaces 2025, 17, 57719−57726

for each reflectance dip, suggests that further improvements are necessary. One route for enhancing the FoM could be achieved by minimizing reflectance dips to nearly zero, which can be done by optimizing resonant light-matter coupling at BPP modes. Another possibility could be the study of bound states in the continuum (BIC) for the present structure, which are known to produce the highest Q values but have never been explored using hyperbolic magnetoplasmonic systems.

3.2. Magnetochiroptical MCD Sensing. Having demonstrated the proposed device's ability to sense achiral analytes through changes in the MCD of reflected circularly polarized light—albeit with a relatively low FoM, we now shift our focus to chiral analytes. Unlike the refractometric sensing approach discussed in the previous section, the case of chiral analytes is more compelling when considering a finite number of particles for two key reasons: (i) it presents a more realistic scenario, and (ii) using a homogeneous chiral superstrate as the analyte induces considerably larger changes in the MCD spectra, even for minimal variations in the refractive index. The latter can be explained by the interaction of the intrinsic chirality of the nanoparticles with the chiral near-fields associated with RCP and LCP modes, inducing much larger changes in the MCD amplitudes. To highlight this effect, rather than applying homogeneous refractive index changes in the superstrate, we now consider a finite number of chiral particles surrounding each MO-HMM cylinder, as illustrated in Figure 5a.

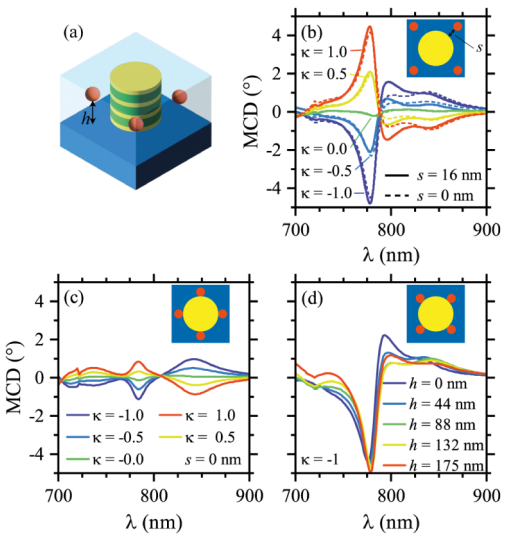

Figure 5. (a) Schematic of four chiral particles (nanospheres) surrounding a unit cell and (b) the enhanced MCD signal in function of κ and s. (c) MCD reduction by changing angular position, but (d) no significant MCD variation by changing the height position.

Specifically, in the first configuration, schematically depicted in Figure 5a, four chiral nanospheres (with diameter of 50 nm) are arranged per unit cell, corresponding to a concentration of 0.44% v/v (volume-to-volume ratio) in the aqueous superstrate. Each nanosphere is positioned at a height h from the substrate, maintaining an equal spacing s from the MO-HMM cylinder. The analyte region (superstrate) is modeled with the refractive index of water (n_a = 1.33), while the nanospheres have a slightly higher refractive index (n_s = 1.34). The use of nanospheres as proxies for chiral molecules is well justified by both numerical and experimental evidence. Studies have shown that the optical interaction with molecules is dictated primarily by their effective volume and refractive index, whereas the precise molecular geometry plays only a secondary role. This principle has been extensively validated in the field of optical forces, as demonstrated in refs[37−39]. As a result, substituting spheres with other geometries of equivalent volume and refractive index leads to only minor variations in the calculated response.[39] Since our primary goal is to quantify MCD in the presence of a chiral analyte medium, we assume that only the nanospheres exhibit chirality, with their optical response described by the constitutive equations in the Boys-Post formulation[40]

$$\boldsymbol{D} = \varepsilon_0 \varepsilon_s \boldsymbol{E} + \mathrm{i}\frac{\kappa}{c}\boldsymbol{B} \tag{5}$$

$$\boldsymbol{H} = \frac{1}{\mu_0}\boldsymbol{B} + \mathrm{i}\frac{\kappa}{c}\boldsymbol{E} \tag{6}$$

where ε_0 and μ_0 are the permittivity and permeability of free space, $\varepsilon_s = n_s^2$ is the permittivity of the chiral nanospheres, c is the speed of light in vacuum, and κ is the chirality factor. Figure 5b shows the remarkable enhancement of MCD in the presence of a chiral medium, considering the set of different values for $\kappa = \{-1, -0.5, 0, +0.5, +1\}$. In particular, for $\kappa = \pm 1$, the highest MCD peaks exceed $\mathrm{MCD_p} > \pm 4°$ around λ = 775 nm, surpassing the refractometric sensing approach by more than 20 times (compare with MCD amplitudes in Figure 4). The maximum difference between MCD peaks for molecules of opposite chirality is given by $\Delta\mathrm{MCD}_{\pm\kappa} = \mathrm{MCD_p}(\kappa = +1) - \mathrm{MCD_p}(\kappa = -1) = 9.42°$, demonstrating exceptional sensitivity. For completeness, additional numerical results for weakly chiral molecules with $\kappa = \pm 0.01$ are provided in Figure S3. Furthermore, we found that varying the nanosphere-cylinder spacing s has negligible effect at λ = 775 nm. This is evident from the nearly identical results for s = 16 nm (solid curves) and s = 0 nm (dashed curves). In contrast, the angular position of the chiral nanospheres around the MO-HMM nanocylinders affects the results significantly. As shown in Figure 5c, rotating the nanospheres by 45° relative to their initial positions leads to a substantial reduction in MCD amplitudes, reaching approximately $\mathrm{MCD_p} \approx \pm 1°$, a corresponding difference of $\Delta\mathrm{MCD}_{\pm 1} = 2.43°$. This effect was obtained for s = 0 nm, i.e., the chiral particles are in contact with the MO-HMM nanocylinder surface. This reduction can be explained by analyzing the near-field distribution in Figure 3a. The maximum near-field amplitudes are concentrated along the diagonal directions —corresponding to the nanosphere positions in the initial configuration. On the other hand, the minimum near-electric field amplitudes are found along the horizontal and vertical midlines of the MO-HMM nanocylinder, corresponding to the nanosphere positions in the rotated configuration. To further verify the position-dependent sensitivity of the MO-HMM nanocylinders to the location of the chiral molecules, we analyzed the effect of varying their vertical position (for s = 0 nm) from h = 0 nm (in contact with the cylinder and substrate) to h = 175 nm (at the cylinder's top surface). Figure 5d shows no significant variations in the MCD peak. Despite the angular dependence of the MCD amplitude—which is controlled precisely in simulations but completely random in experiments—our analysis reveals that the proposed approach has strong potential for detecting very low concentrations of chiral nanoparticles. Moreover, experimental studies have demonstrated that near-field optical gradients generate optical forces that attract particles toward

https://doi.org/10.1021/acsami.5c16043
ACS Appl. Mater. Interfaces 2025, 17, 57719−57726

regions of maximum field intensity.[41] This phenomenon drives nanoparticles toward high-field concentration regions, further reinforcing the viability of our approach for detecting ultralow concentrations of chiral nanoparticles. It is worth noting that a concentration of four nanospheres per unit cell represents an intermediate level —not particularly low, yet not excessively high. As previously discussed, increasing the number of nanoparticles enhances the interaction between the intrinsic chirality of matter (as described by eqs 5−6 and the chiral near-fields. Consequently, this leads to higher observed MCD amplitudes. Conversely, when the molecular concentration is low or the molecules themselves are very small, the interaction with the chiral near field becomes significantly weaker. This is illustrated in Figure S4, which considers a configuration comprising four 10 nm chiral molecules per unit cell. Despite the reduced MCD signal in this scenario, the chiral molecules remain detectable. We also performed simulations for four chiral nanospheres of 50 nm with a refractive index of $n_s = 1.44$ to emulate the electromagnetic properties of α-synuclein amyloid fibrils.[42] These fibrils are biologically and clinically relevant chiral proteins implicated in neurodegenerative disorders such as Parkinson's disease and prion-related conditions. In the absence of experimental data for the chiral parameter κ, simulations were conducted across a plausible range of κ values to evaluate the system's sensitivity. For comparison, results obtained for $n_s = 1.34$ show only minor differences in the MCD response, as illustrated in Figure S5. This outcome highlights the robustness of our platform and its potential, when combined with suitable surface functionalization, to detect a wide range of chiral molecules at extremely low concentrations, including the single-molecule limit. Such capability supports both the experimental feasibility and the broad applicability of our proposal.

To provide numerical evidence to support the previous claims, we will now proceed to validate the capability of the proposed concept for detecting ultralow concentrations—including the extreme case of a single molecule per unit cell. We analyze two specific scenarios: two nanospheres (a concentration of 0.22% v/v) in Figure 6a and a single nanosphere (a concentration of 0.11% v/v) in Figure 6b. In both cases, the nanoparticles are positioned at half the height of the MO-HMM cylinder and assigned a chirality factor of $\kappa = -1$. The nanospheres are then rotated around the cylinder by an angle ϕ, as illustrated in the inset. In the first case, two nanospheres are rotated simultaneously by the same angle within the range $0° \le \phi \le 150°$, while maintaining opposite positions relative to the cylinder. In the second case, the single nanosphere is rotated within a range of $0° \le \phi \le 360°$. Figure 6a for the two-nanosphere case shows MCD spectra with a pronounced peak around $\lambda = 775$ nm, with variations observed only in the peak magnitude rather than its spectral position. Figure 6b presents a density plot of the MCD as a function of λ and ϕ for a single chiral nanosphere. Here, the MCD peak exhibits fluctuations, which, as discussed previously, arise from the molecule's positioning in regions of high and low near-electric field amplitudes. Notably, two chiral hotspots appear in the range $150° \le \phi \le 210°$, where the MCD peaks transition from negative to positive values. These hotspots arise from two key contributions: (i) the oblique incidence of light, which induces inhomogeneous near-field distributions, as also evidenced in Figure 3, and (ii) chiral light-matter interactions of the near-fields with the single nanosphere. Though the MCD response varies with ϕ—a limitation that could be inherently mitigated by induced gradient optical forces—our analysis highlights the remarkably high MCD peaks, reaching values up to $MCD_p = -2.36°$. This value represents a significant enhancement compared to conventional MCD responses, which are typically reported in the range of a few tens or even single-digit millidegrees.[43] This substantial amplification confirms the effectiveness of the metasurface design for chiral molecule detection, regardless of the analyte's position around the nanodisk. Indeed, it enables the detection of chiral species down to the single-nanoparticle-per-unit-cell level, which is the fundamental detection limit of our proposal.

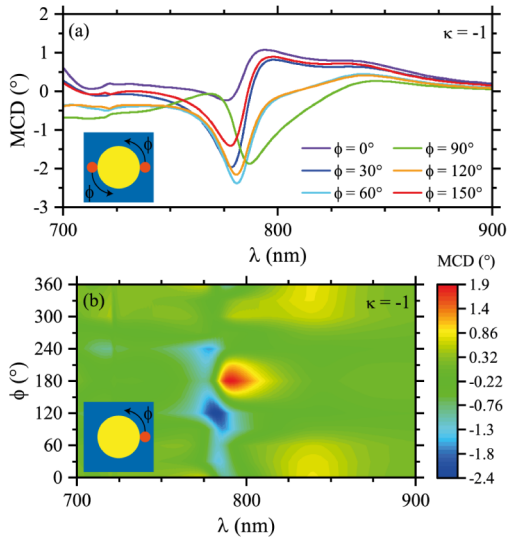

Figure 6. (a) MCD curves for only two particles and (b) MCD density plot for a single particle with $\kappa = -1$ and $s = 0$ nm, as a function of rotation angle ϕ and wavelength λ.

4. CONCLUSION

This study introduces a novel optical metasurface based on MO-HMM nanodisks, offering a powerful platform for MCD-based biosensing. Engineered from alternating layers of metallic and MO dielectric materials, the metasurface functions as a two-dimensional grating that eliminates the need for bulky prism coupling. Under phase-matching conditions, it enables efficient coupling of light into BBP modes. Our results demonstrate the exceptional versatility and sensitivity of this platform for both refractometric and chiroptical sensing. In refractometric mode, the metasurface achieves a linear MCD sensitivity of $S = 245$ nm·RIU^{-1}, indicating strong responsiveness to refractive index changes in achiral analytes. In chiroptical mode, it detects chiral molecules at remarkably low concentrations, with MCD peak signals reaching $|MCD_p| = 2.71°$, $|MCD_p| = 2.41°$, and $|MCD_p| = 2.36°$ for concentration ratios of four, two, and one molecule per unit cell, respectively. These results reveal not only the system's exceptional chiral selectivity but also its capability to operate at the edge of the detection limit. A particularly striking outcome is the 20-fold enhancement in MCD response enabled by the extrinsic chirality of the MO-HMM nanodisk structure—a significant advance for label-free detection of both achiral and chiral species. Most notably, our simulations confirm the ability to detect chiral molecules at the single-nanoparticle-per-unit-cell level, representing the lowest possible analyte concentration achievable in numerical simulations of such a system.

https://doi.org/10.1021/acsami.5c16043
ACS Appl. Mater. Interfaces 2025, 17, 57719−57726

Altogether, these findings establish our concept as a groundbreaking biosensing platform that combines high sensitivity, compact design, and chiral selectivity. This advancement opens new avenues for label-free, ultrasensitive detection of chiral molecules in biological, pharmaceutical, and diagnostic applications, where precision at the low molecular-concentration scale is increasingly critical.

■ ASSOCIATED CONTENT

Data Availability Statement

Data underlying the results presented in this paper are not publicly available at this time but may be obtained from the authors upon reasonable request.

Supporting Information

The Supporting Information is available free of charge at https://pubs.acs.org/doi/10.1021/acsami.5c16043.

Simulation results for CD signals at different θ_{inc} angles, along with an analysis considering a low chirality factor ($\kappa = \pm 0.01$), a small molecule size (10 nm diameter), and nanospheres emulating α-synuclein amyloid fibril molecules (PDF)

■ AUTHOR INFORMATION

Corresponding Authors

William O F Carvalho − *National Institute of Telecommunications (Inatel), Santa Rita Do Sapucaí, Minas Gerais 37536-001, Brazil;* orcid.org/0000-0001-6178-0061; Email: william.orivaldo@inatel.br

Jorge R Mejía-Salazar − *National Institute of Telecommunications (Inatel), Santa Rita Do Sapucaí, Minas Gerais 37536-001, Brazil;* orcid.org/0000-0003-1742-9957; Email: jrmejia@inatel.br

Authors

Ana L Lyra Pavanelli − *National Institute of Telecommunications (Inatel), Santa Rita Do Sapucaí, Minas Gerais 37536-001, Brazil*

Osvaldo N. Oliveira, Jr. − *Sao Carlos Institute of Physics, University of Sao Paulo, São Carlos, São Paulo 13560-970, Brazil;* orcid.org/0000-0002-5399-5860

Complete contact information is available at: https://pubs.acs.org/10.1021/acsami.5c16043

Notes

The authors declare no competing financial interest.

■ ACKNOWLEDGMENTS

This work has been funded by the following research projects: Brazil 6G Project with support from RNP/MCTI (Grant 01245.010604/2020-14), xGMobile Project code XGM-AFCCT-2024-7-9-1 with resources from EMBRAPII/MCTI (Grant 052/2023 PPI IoT/Manufatura 4.0 and FAPEMIG Grant PPE-00124-23). We also acknowledge financial support from the Brazilian agency National Council for Scientific and Technological Development-CNPq (308068/2025-4, 405014/2025-2), FAPESP (2018/22214-6), and FAPEMIG (APQ-04523-23).

■ REFERENCES

(1) McConathy, J.; Owens, M. J. Stereochemistry in Drug Action. *Prim. Care Companion J. Clin. Psychiatry.* **2003**, *5*, 70−73.

(2) Renslo, A. *In The Organic Chemistry of Medicinal Agents*, Renslo, A., Ed.; McGraw-Hill Education: New York, NY, 2016.

(3) Dobson, C. M. Protein folding and misfolding. *Nature* **2003**, *426*, 884−890.

(4) Mohammadi, E.; Tsakmakidis, K.; Askarpour, A.-N.; Dehkhoda, P.; Tavakoli, A.; Altug, H. Nanophotonic platforms for enhanced chiral sensing. *ACS Photonics* **2018**, *5*, 2669−2675.

(5) Tokunaga, E.; Yamamoto, T.; Ito, E.; Shibata, N. Understanding the Thalidomide Chirality in Biological Processes by the Self-disproportionation of Enantiomers. *Sci. Rep.* **2018**, *8*, 17131.

(6) Francés-Soriano, L.; Zaballos-García, E.; Pérez-Prieto, J. Up- and Down-Shifting Nanomaterials with Chiroptical Responses: Origin of their Chiroptical Activity and Applications. *Adv. Opt. Mater.* **2023**, *11*, 2300337.

(7) Zhang, N.-N.; Shen, Z.-L.; Gao, S.-Y.; Peng, F.; Cao, Z.-J.; Wang, Y.; Wang, Z.; Zhang, W.; Yang, Y.; Liu, K.; et al. Synthesis and Plasmonic Chiroptical Properties of Double-Helical Gold Nanorod Enantiomers. *Adv. Opt. Mater.* **2023**, *11*, 2203119.

(8) Nesterov, M. L.; Yin, X.; Schäferling, M.; Giessen, H.; Weiss, T. The Role of Plasmon-Generated Near Fields for Enhanced Circular Dichroism Spectroscopy. *ACS Photonics* **2016**, *3*, 578−583.

(9) Beyrami, H.; Golshan, M.; Kucińska-Lipka, J.; Saeb, M. R.; Salami-Kalajahi, M. Chiral-based optical and electrochemical biosensors: Synthesis, classification, mechanisms, nanostructures, and applications. *Chem. Eng. J.* **2024**, *497*, 155562.

(10) Paiva-Marques, A. W.; Reyes Gómez, F.; Oliveira, O. N., Jr.; Mejía-Salazar, J. R. Chiral plasmonics and their potential for point-of-care biosensing applications. *Sensors* **2020**, *20*, 944.

(11) Besteiro, L. V.; Liu, Y.; Okamoto, H. Chirality of plasmonic structures and materials. *J. Chem. Phys.* **2024**, *161*, 180401.

(12) Ahn, H.-Y.; Le, K. Q.; Narushima, T.; Yamanishi, J.; Kim, R. M.; Nam, K. T.; Okamoto, H. Highly Chiral Light Emission Using Plasmonic Helicoid Nanoparticles. *Adv. Opt. Mater* **2024**, *12*, 2400699.

(13) Tan, L.; Fu, W.; Gao, Q.; Wang, P.-P. Chiral Plasmonic Hybrid Nanostructures: A Gateway to Advanced Chiroptical Materials. *Adv. Mater.* **2024**, *36*, 2309033.

(14) Lim, Y.-C.; Kim, R. M.; Han, J. H.; Aharonovich, I.; Nam, K. T.; Kim, S. Strong Chiral Response of Chiral Plasmonic Nanoparticles to Photonic Orbital Angular Momentum. *Adv. Opt. Mater.* **2025**, *13*, 2402268.

(15) Ma, X.; Liu, S.; Ji, Y.; Ma, S.; Jiang, J.; Zhang, L.; Wu, X.; Li, J.; Liu, M.; Wang, R.-Y. Chiral Amplifier With Highly Tunable Plasmonic Optical Activities for Molecular Chirality Sensing. *Adv. Mater. Technol.* **2025**, *10*, 2401435.

(16) Indukuri, S. C.; Frydendahl, C.; Sharma, N.; Mazurski, N.; Paltiel, Y.; Levy, U. Enhanced chiral sensing at the few-molecule level using negative index metamaterial plasmonic nanocuvettes. *ACS Nano* **2022**, *16*, 17289−17297.

(17) Zhang, C.; Hu, H.; Ma, C.; Li, Y.; Wang, X.; Li, D.; Movsesyan, A.; Wang, Z.; Govorov, A.; Gan, Q.; et al. Quantum plasmonics pushes chiral sensing limit to single molecules: a paradigm for chiral biodetections. *Nat. Commun.* **2024**, *15*, 2.

(18) Qin, J.; Deng, L.; Kang, T.; Nie, L.; Feng, H.; Wang, H.; Yang, R.; Liang, X.; Tang, T.; Shen, J.; Li, C.; Wang, H.; Luo, Y.; Armelles, G.; Bi, L. Switching the Optical Chirality in Magnetoplasmonic Metasurfaces Using Applied Magnetic Fields. *ACS Nano* **2020**, *14*, 2808−2816.

(19) Fan, F.; Zhong, C.; Zhang, Z.; Li, S.; Chang, S. Terahertz chiral sensing and magneto-optical enhancement for ferromagnetic nanofluids in the chiral metasurface. *Nanoscale Adv.* **2021**, *3*, 4790−4798.

(20) Tan, Z.; Fan, F.; Zhao, D.; Ji, Y.; Cheng, J.; Chang, S. High-Efficiency Terahertz Nonreciprocal One-Way Transmission and Active Asymmetric Chiral Manipulation Based on Magnetoplasmon/Dielectric Metasurface. *Adv. Opt. Mater.* **2021**, *9*, 2002216.

(21) Ignatyeva, D. O.; Krichevsky, D. M.; Belotelov, V. I.; Royer, F.; Dash, S.; Levy, M. All-dielectric magneto-photonic metasurfaces. *J. Appl. Phys.* **2022**, *132*, 100902.

(22) Li, W.; Yang, Q.; You, O.; Lu, C.; Guan, F.; Liu, J.; Shi, J.; Zhang, S. Magneto-optical chiral metasurfaces for achieving polarization-independent nonreciprocal transmission. *Sci. Adv.* **2024**, *10*, No. eadm7458.
(23) Ye, S.; Zhang, X.; Chang, L.; Wang, T.; Li, Z.; Zhang, J.; Yang, B. High-Performance Plasmonic Sensors Based on Two-Dimensional Ag Nanowell Crystals. *Adv. Opt. Mater.* **2014**, *2*, 779−787.
(24) Mejía-Salazar, J. R.; Oliveira, O. N., Jr. Plasmonic Biosensing. *Chem. Rev.* **2018**, *118*, 10617−10625.
(25) Lambert, A. S.; Valiulis, S. N.; Malinick, A. S.; Tanabe, I.; Cheng, Q. Plasmonic Biosensing with Aluminum Thin Films under the Kretschmann Configuration. *Anal. Chem.* **2020**, *92*, 8654−8659.
(26) Hu, R.; Lin, S.; Li, F.; Shen, J.; Xie, Y.; Deng, B.; Zhang, Y.; Dong, Z.; Zhu, J. Exploring Aptamer-Based Metasurfaces for Label-Free Plasmonic Biosensing of Breast Tumor-Derived Exosomes. *Adv. Opt. Mater.* **2024**, *12*, 2401180.
(27) Tukova, A.; Nguyen, N. T. T.; Garcia-Bennett, A.; Rodger, A.; Wang, Y. Plasmonic Nanostars: Unique Properties That Distinguish Them from Spherical Nanoparticles from a Biosensing Perspective. *Adv. Opt. Mater* **2024**, *12*, 2401183.
(28) Carvalho, W. O. F.; Oliveira, O. N., Jr.; Mejía-Salazar, J. R. Magnetochiroptical nanocavities in hyperbolic metamaterials enable sensing down to the few-molecule level. *J. Chem. Phys.* **2024**, *160*, 071104.
(29) Kuttruff, J.; Gabbani, A.; Petrucci, G.; Zhao, Y.; Iarossi, M.; Pedrueza-Villalmanzo, E.; Dmitriev, A.; Parracino, A.; Strangi, G.; De Angelis, F.; Brida, D.; Pineider, F.; Maccaferri, N. Magneto-Optical Activity in Nonmagnetic Hyperbolic Nanoparticles. *PRL* **2021**, *127*, 217402.
(30) Kim, T. C.; Ojha, S.; Tian, G.; Lee, S. H.; Jung, H. K.; Choi, J. W.; Kornblum, L.; Walker, F. J.; Ahn, C. H.; Ross, C. A.; et al. Self-assembled multiferroic epitaxial $BiFeO_3$–$CoFe_2O_4$ nanocomposite thin films grown by RF magnetron sputtering. *J. Mater. Chem. C* **2018**, *6*, 5552−5561.
(31) Zhang, Y.; Wang, C.; Liang, X.; Peng, B.; Lu, H.; Zhou, P.; Zhang, L.; Xie, J.; Deng, L.; Zahradnik, M.; et al. Enhanced magneto-optical effect in thin films deposited on silicon by pulsed laser deposition. *J. Alloys Compd.* **2017**, *703*, 591−599.
(32) Onbasli, M. C.; Beran, L.; Zahradník, M.; Kučera, M.; Antoš, R.; Mistrík, J.; Dionne, G. F.; Veis, M.; Ross, C. A. Optical and magneto-optical behavior of Cerium Yttrium Iron Garnet thin films at wavelengths of 200−1770 nm. *Sci. Rep.* **2016**, *6*, 23640.
(33) Johnson, P. B.; Christy, R. W. Optical constants of the noble metals. *Physical Rev. B* **1972**, *6*, 4370.
(34) Malitson, I. H. Interspecimen comparison of the refractive index of fused silica. *J. Opt. Soc. Am.* **1965**, *55*, 1205−1209.
(35) Poddubny, A.; Iorsh, I.; Belov, P.; Kivshar, Y. Hyperbolic metamaterials. *Nat. Photonics* **2013**, *7*, 948−957.
(36) Diaz-Valencia, B. F.; Porras-Montenegro, N.; Oliveira, O. N., Jr.; Mejía-Salazar, J. R. Nanostructured hyperbolic metamaterials for magnetoplasmonic sensors. *ACS Appl. Nano Mater.* **2022**, *5*, 1740−1744.
(37) Yoo, D.; Gurunatha, K. L.; Choi, H.-K.; Mohr, D. A.; Ertsgaard, C. T.; Gordon, R.; Oh, S.-H. Low-power optical trapping of nanoparticles and proteins with resonant coaxial nanoaperture using 10 nm gap. *Nano Lett.* **2018**, *18*, 3637−3642.
(38) Hernández-Sarria, J. J.; Oliveira, O. N., Jr.; Mejía-Salazar, J. R. Toward lossless infrared optical trapping of small nanoparticles using nonradiative anapole modes. *Phys. Rev. Lett.* **2021**, *127*, 186803.
(39) Hernandez-Sarria, J. J.; Oliveira, O. N., Jr.; Mejía-Salazar, J. R. Numerical simulations of double-well optical potentials in all-dielectric nanostructures for manipulation of small nanoparticles in aqueous media. *ACS Appl. Nano Mater.* **2023**, *6*, 1405−1412.
(40) Klimov, V. V.; Zabkov, I. V.; Pavlov, A. A.; Guzatov, D. V. Eigen oscillations of a chiral sphere and their influence on radiation of chiral molecules. *Opt. Express* **2014**, *22*, 18564−18578.
(41) Wang, K.; Schonbrun, E.; Steinvurzel, P.; Crozier, K. B. Trapping and rotating nanoparticles using a plasmonic nano-tweezer with an integrated heat sink. *Nat. Commun.* **2011**, *2*, 469.
(42) Smith, R. A. S.; Nabok, A.; Blakeman, B. J. F.; Xue, W.-F.; Abell, B.; Smith, D. P. Analysis of toxic amyloid fibril interactions at natively derived membranes by ellipsometry. *PLoS One* **2015**, *10*, No. e0132309.
(43) Ngamdee, K.; Ngeontae, W. Circular dichroism glucose biosensor based on chiral cadmium sulfide quantum dots. *Sens. Actuators, B* **2018**, *274*, 402−411.

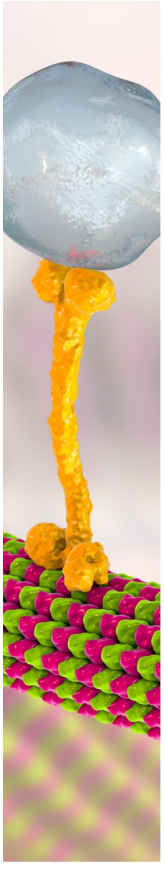

https://doi.org/10.1021/acsami.5c16043
ACS Appl. Mater. Interfaces 2025, 17, 57719−57726